East European Journal of Physics. **1.** 247-255 (2026)
DOI:10.26565/2312-4334-2026-1-27 ISSN 2312-4334

# INVESTIGATION OF THE PHYSICAL PROPERTIES OF $Yb^{3+}$ DOPED $ZnFe_2O_4$ NANOPOWDERS SYNTHESIZED BY SOL GEL METHOD

**M. Guettaf[1]*, S. Saadi[2], D. Mouattah[3], A. Kezzim[1], I. Lanez[1], B. Rekik[1]**
*[1]Laboratory of Physical-Chemical Inorganic Materials and their applications (LPCMIA), Saad Dahleb University-Blida 1, BP270 09000, Blida, Algeria*
*[2]Laboratory of Applied Chemistry and Materials (LabCAM), University of M'hamed Bougara of Boumerdes, Avenue de l'Indépendance, Boumerdes, 35000. Algeria*
*[3]Laboratory Physico- Chemistry of Materials (LPCM), University of Amar Telidji, BP37G 03000, Laghouat, Algeria*
**Corresponding author e-mail:* guettaf_mohamed@univ-blida.dz

Received July 7, 2025; revised December 20, 2025; accepted January 16, 2026

$ZnFe_{2-x}Yb_xO_4$ with (x = 0, 0.01, 0.02, 0.03, 0.05, 0.07, and 0.09) have been successfully synthesized by the sol-gel method at 750°C. X-ray diffraction results showed a single phase and crystalline nanopowders of spinel-type structure with cubic symmetry and space group. The lattice parameters increase with $Yb^{3+}$ concentrations. The BET specific area of $ZnxFe_{2-x}Yb_xO_4$ (x = 0.03) was determined to be the larger 13.59 $m^2/g$. The crystallite size was determined by Rietveld to be in the range of 29-104 nm. FTIR spectra showed two strong absorption bands, a common characteristic of the spinel structure. Further, the shifting of the lower absorption band toward a higher frequency confirms that $Yb^{3+}$ ions predominantly replaced $Fe^{3+}$ ions in octahedral sites. The formation of the spinel phase in the samples was also validated by Raman scattering, with asymmetric broadening, and a systematic shift in the Raman spectra was observed as a function of Yb3+ concentration. Scanning electron microscopy SEM showed that powders consist of micrometric aggregation of smaller particles. EDS examinations verified that the chemical elements Zn, Fe, Yb, and O are present in all samples. The direct bandgap energy values are calculated by Tauc's plot, and it indicates a semiconductor character of our compound, revealing an increase and enhancement in bandgap energy values from 1.82 to 2.4 eV with $Yb^{3+}$ substitution.

**Keywords:** *Ytterbium; Zinc ferrite nanopowders; XRD; Raman; Bandgap energy*
**PACS:** 75.50.Gg , 78.20.-e, 81.20.Fw

## 1. INTRODUCTION

The synthesis of nanostructured materials with controlled composition and improved chemical-physical properties is one of the most interesting fields of materials science. Spinel compounds with excellent chemical stability and optical properties have attracted the attention of many researchers in various technological applications such as cancer treatment [1], medicinal chemistry and pharmacology [2,3], photo catalyst in wastewater treatment [4-6] $H_2$-generation under visible irradiation [7, 8], lithium-ion batteries [9-11] and gas-sensing devices [12,13]. The spinel ferrite oxides are a new family of magnetic nanomaterials, in which ferric ions "$Fe^{3+}$" play a prominent role as a principal cation in their composition [14]. This family of magnetic nanoparticles shows impressive properties which proved to be promising nanomaterials used in a variety of magnetic applications such as magnetic resonance imaging [15,16] and magnetic hyperthermia [17, 18]. The molecular formulas of spinel ferrites are represented by $MFe_2O_4$ (M is a divalent ion, such as $Ni^{2+}$, $Mg^{2+}$, $Zn^{2+}$, $Co^{2+}$, etc.). The unit cell has two distinct internal sites with a total of 96 sites, of which 64 are tetrahedral A-sites and 32 are octahedral B-sites. The structure attributes of spinel ferrites are intricately influenced by magnetic interactions and the distribution of cations across B and A sites [19]. Zinc ferrite bulk material $ZnFe_2O_4$ has a normal spinel structure, where divalent cations $Zn^{2+}$are located on the tetrahedral sites while trivalent cations $Fe^{3+}$ are located at the octahedral sites [20]. Zinc ferrite nanoparticles doped with transition metals are being studied widely by various research groups [21-23]. Recently, the substitution of rare-earth elements in zinc ferrite was also studied in numerous research such as ytterbium ($Yb^{3+}$), Neodymium ($Nd^{3+}$) Lutetium ($Lu^{3+}$) substitution [24-26]. Rare earth ions are one of the most excellent substituents to further improve zinc ferrite properties. They play a major part in the enrichment of their electromagnetic characteristics [27,28]. Trivalent rare-earth dopants prefer a cubic crystallization system occupying the octahedral sites due to their larger ionic radius [29]. In fact, the ionic radius of rare earth elements is larger than $Fe^{3+}$ which leads to a structural distortion of the spinel ferrite [30]. The substitution of the host iron ion (3d) in coordination number CN = 8 by rare earth cations (4f) results in structural distortions and thus significantly modifying the structural properties and optical ones of the ferrite nanoparticles through the coupling of the 3d-4f electron [31].

The aim of this study is to synthesize $ZnFe_{2-x}Yb_xO_4$ with x= 0, 0.02, 0.03, 0.05, 0.07, and 0.09 pure phase using the sol-gel method at 750°C. The works ought to improve structural, morphological and optical properties via $Yb^{3+}$-substitution process. Extensive characterization with various technics including XRD, FTIR, BET, SEM and diffuse reflectance were interested in investigating the impact of ytterbium concentrations on enhancement bandgap energy of the $ZnFe_{2-x}Yb_xO_4$ compounds.

---

***Cite as:*** M. Guettaf, S. Saadi, D. Mouattah, A. Kezzim, I. Lanez, B. Rekik, East Eur. J. Phys. 1, 247 (2026), https://doi.org/10.26565/2312-4334-2026-1-27

## 2. EXPERIMENTAL

### 2.1. Synthesis

$Yb^{3+}$ doped $ZnFe_2O_4$ were synthesized by sol-gel method using zinc nitrate $Zn(NO_3)_2.6H_2O$, iron nitrate $Fe(NO_3)_3.9H_2O$ purchased from Alfa Aesar. Ytterbium nitrate $Yb(NO_3)_3.5H_2O$ with 99.9 % and citric acid $C_6H_8O_7$ were supplied from Sigma-Aldrich with 99.9% purity. First, $Zn(NO_3)_2.6H_2O$, $Fe(NO_3)_39.H_2O$, and $Yb(NO_3)_3.5H_2O$, in their respective stoichiometry were dissolved in 10 mL of deionized water which were then mixed. After continuous stirring for 30 min at room temperature, a citric acid $C_6H_8O_7$, as a complexity agent, was added to the solution which was then heated at 85°C under magnetic stirring until a gel formed. The resultant gel was dried at 80 °C for 48 hours. Then, the generated powders were ground in an agate mortar and heat-treated at 750 °C for 8 hours in a tube oven in the air (4 h, 5 °C/min). The procedure is illustrated in figure 1.

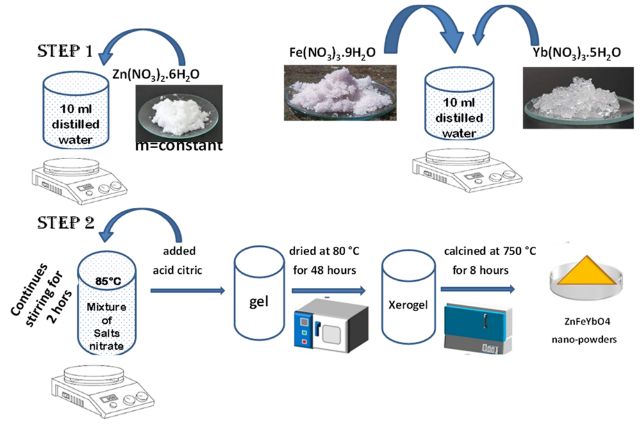

**Figure 1.** Different steps of synthesis of $ZnFe_{2-x}Yb_xO_4$ (x=0 0.01 0.02, 0.03 0.05 0.07 and 0.09) nanoparticles by sol-gel method

### 2.2 Characterizations

The identifications of $ZnFe_{2-x}Yb_xO_4$ phases were done by using X-ray diffraction (XRD). The patterns were recorded with Brüker D8 Phaser X-ray diffractometer equipped with Cu Kα radiation (λCu = 1.5418 Å) in the 2θ range (10–70°). Raman spectra for samples were recorded on a Horiba Jobin Yvon Lab Ram high-resolution spectrometer in backscattering geometry in the range 100–1000 $cm^{-1}$ with a He-Ne laser excited with wavelength 532nm, grating 1800 lines/mm, slit 100, power at sample of 0.4 and 1.0 mW, and acquisition 20 s/5 cycles. Jasco FT/IR-4200 was used for Fourier Transform Infrared spectroscopy over the range 400–4000 $cm^{-1}$.The morphology of the nanopowders was investigated using a scanning electron microscope (SEM-EDS) on a Quattro SEM FEG. The BET surface area, pore-volume and pore size distributions were investigated via $N_2$ sorption performed on a BET ASAP 2020 PLUS 2.00 instrument. The grain size distribution was measured using the Mastersizer 2000, Malvern laser instrument. The different grain sizes were dispatched among various classes and used to evaluate the most relevant statistical diameters. The band gap energies Eg of the $ZnFe_{2-x}Yb_xO_4$ nanomaterials were determined from the Tauc relation using the diffuse reflectance data recorded on a optima SP-3000nano spectrophotometer between (200–800 nm.

## 3. RESULTS AND DISCUSSIONS

### 3.1. Structural properties

XRD patterns of $Yb^{3+}$ doped $ZnFe_2O_4$ samples synthesized at 750°C using sol-gel method are shown in Figure 2a. The results indicate that all the samples crystallize in a cubic spinel structure according to JCPDS card no. 22-1012 with the space group: Fd-3m [32,33]. All diffraction peaks were indexed and matched to a single phase without the detection of any peaks attributed to the formation of secondary phases. As a result, $Yb^{3+}$ atoms are assumed to be efficiently incorporated into the lattice within the studied range. Figure 2b shows that the $Yb^{3+}$ substitution causes a shift of the XRD peaks towards to the lower diffraction angles values. The extent of the peak shift is dependent on the $Yb^{3+}$ content. The same behaviour was observed upon substituting Yb3+ in cobalt ferrite nanoparticles [34]. This may be attributed to the ionic radius of Yb3+ (0,85 Å), which is larger than that of Fe3+ (0,64 Å), causing an increase in the interplanar spacing and a subsequent decrease in the diffraction angle as the lattice parameter increases [35].

Beyond a certain concentration of $Yb^{3+}$, the single-phase domain of the solid solution becomes poly-phase by the appearance of new peaks due to the high $Yb^{3+}/Fe^{3+}$ ratio, indicating the formation of secondary phases ytterbium oxide ($Yb_2O_3$) and ytterbium iron perovskite ($YbFeO_3$), which crystallized in cubic phase (JCPDS file no. 43-1037) and orthorhombic structure (JCPDS file no. 047-0070) respectively. We are confirmed by preparing samples with higher concentrations of $Yb^{3+}$ showing that the limiting solubility for this compound is when the concentration of $Yb^{3+}$ is located belongs to 10% and 20% (Figure 2c). Consequently, it can be seen that the maximum solubility limit of $Yb^{3+}$ ions in the $ZnFe_2O_4$ crystal structure lies between 10% and 20%.

The lattice parameter *a* is sensitive to the composition of the solid solution (Figure 3). At first sight, the substitution of $Yb^{3+}$ with greater ionic radii in place of $Fe^{3+}$ at octahedral site causes expansion of crystalline structure which resulted into increase in lattice parameters. However, a close examination reveals that a x = 0, 0.01 and 0.02 concentrations are formed, indicating that the parameter *a* is not affected by the little amount of $Yb^{3+}$ substitution, and then a decrease at x=0.05 after which it increases and reaches a maximum at x = 0.09. The lattice parameters are calculated by Rietveld refinement program. Clearly, the lattice parameter of the doped samples is higher than that of the undoped original compound and increases with increasing $Yb^{3+}$ incorporation. This behavior is associated with the larger ionic radius of ytterbium (r=0.87A°) in octahedral coordination compared to iron (r=0.65A°). The considerable difference in ionic radii between $Yb^{3+}$ and $Fe^{3+}$ leads to a deviation from Vegard's law, which explains the non-linear increase in the lattice parameter with increasing dopant concentration [36].

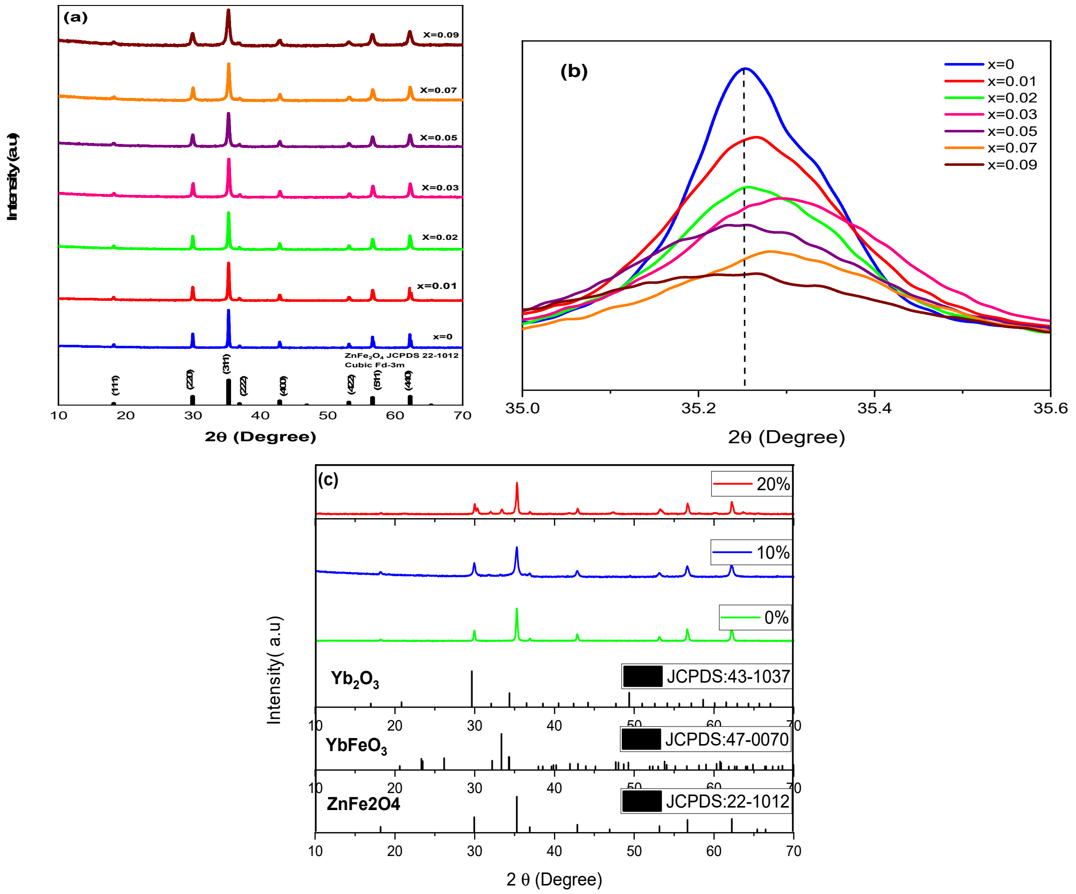

**Figure 2.** (a) X-ray diffraction patterns of $ZnFe_{2-x}Yb_xO_4$ (x= 0, 0.01, 0.02, 0.03, 0.05, 0.07, and 0.09), (b) expanded view of 2θ diffraction peak between 35 and 35.6, and (c) the solubility limit of $Yb^{3+}$ ions in $ZnFe_2O_4$ nanopowders

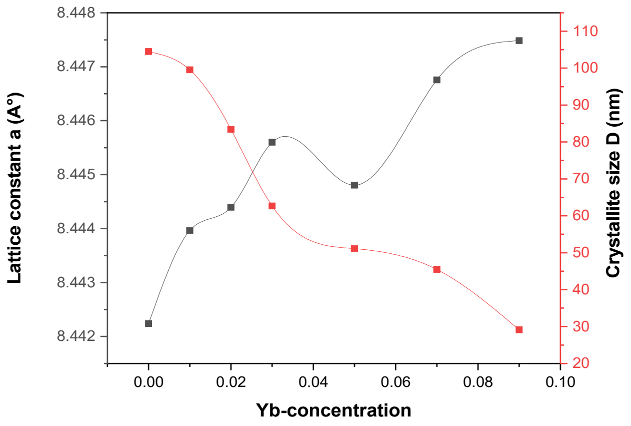

**Figure 3**. Composition dependence of the lattice parameters and crystallite size (D) of $ZnFe_{2-x}Yb_xO_4$ (x=0, 0.01, 0,02,0.03, 0.05, 0.07, 0.09)

The calculated values for the lattice constant (a) and cell volume (V) are shown in Table 1. The obtained values of the lattice constant (a = 8.442 Å), for $ZnFe_2O_4$ (x=0) are in good agreement with the earlier reported values (a = 8.44 Å) [37, 38].

**Table 1.** Lattice parameters, Crystallite size, cell volume and surface area of $ZnFe_{2-x}Yb_xO_4$ compounds

| x | Lattice constant *a* (A°) | cell volume *V*(A°³) | Crystallite size *D Rietveld refinement* (nm) | Crystallite size *D Scherrer* (nm) | XRD density *ρ* (g/ cm³) | $S_{BET}$ (exp) (m²/g) | $D_{BET}$ (nm) |
|---|---|---|---|---|---|---|---|
| 0 | 8.44224 | 601.690 | 104.49645 | 70.025 | 5.33 | 6.415 | 175.47 |
| 0.01 | 8.44397 | 602.060 | 99.57471 | 44.962 | 5.35 | / | / |
| 0.02 | 8.4444 | 602.152 | 83.40205 | 43.137 | 5.38 | / | / |
| 0.03 | 8.4456 | 602.409 | 62.64066 | 32.075 | 5.40 | 13.589 | 81.765 |
| 0.05 | 8.44481 | 602.240 | 51.09478 | 27.275 | 5.43 | / | / |
| 0.07 | 8.44676 | 602.657 | 45.45637 | 30.062 | 5.50 | 11.388 | 95.794 |
| 0.09 | 8.44749 | 602.813 | 29.09815 | 18.85 | 5.55 | / | / |

In Table 1 is also shown the average crystallite size ($D_{XRD}$) which are evaluated from the width at mid-height β (β, radians) of the most intense peak using Debye Scherrer's formula [39]:

$$D = \frac{k\lambda}{\beta \cdot cos\theta}. \tag{1}$$

Where is a shape factor (taken as 0.94 for spherical crystallites), λ represents the X-ray wavelength, and θ signifies Bragg's angle. Moreover, crystallite size D was calculated by the Rietveld method, and by comparison with Scherer, the Rietveld method appeared to give better results.

As a results, $Yb^{3+}$ content increases, the diameter is also found to decrease due to the larger ionic radii of the dopant. The average crystallite sizes were found to be between 29 and 104 nm. The theoretical value of X-ray density ρ (as mentioned in Table 1) increases as the $Yb^{3+}$ concentration increases in the samples, and it was calculated through the following formula:

$$\rho = \frac{8M}{N_A a^3}. \tag{2}$$

Where a is the lattice parameter, $N_A$ represents Avogadro's number, and M indicates the molecular weight of the synthesized samples.

To determine the specific surface area and the pore size distribution of the synthesized samples, we have used the BET method. According to the nitrogen sorption data, the surface areas of $ZnFe_2O_4$ replaced with $Yb^{3+}$ at composition values of 0, 0.03, and 0.07 is 6.415, 13.589, and 11.388 m²/g, respectively. Specific surface area is highly affected by the substitution ratio. The highest surface area is attributed to the sample with composition x = 0.03 with a value of 13.589 m²/g. whereas the average particle size $D_{BET}$, was determined using the following formula:

$$D_{BET} = \frac{6}{\rho \times s_{BET}}. \tag{3}$$

It should be noted that the sample with x = 0.03 has the smallest average particle size (81.765 nm, from Table 1) compared to x = 0 and 0.07. This confirms that the specific surface area and the particle size are inversely related to each other [40].

### 3.2. Vibrational properties

In order to explain the cation distribution at tetrahedral and octahedral sites in ferrites samples which are known to be sensitive to infrared in the 400-700 cm⁻¹ range where the characteristic metal-oxygen bands appear [41]. Figure 4 shows FTIR spectra of the $ZnYb_xFe_{2-x}O_4$ nanopowders after calcination at 750°C.

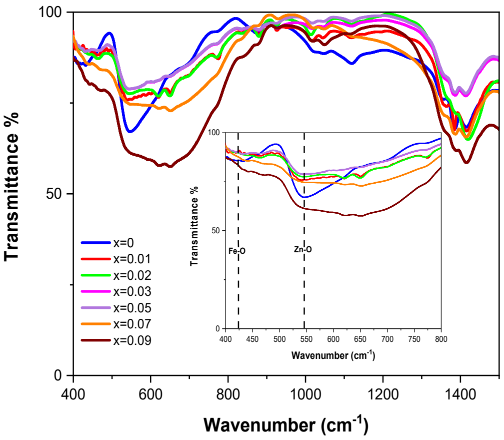

**Figure 4.** FTIR spectra $ZnFe_{2-x}Yb_xO_4$ (x = 0, 0.01, 0.02, 0.03, 0.05, 0.07, and 0.09)

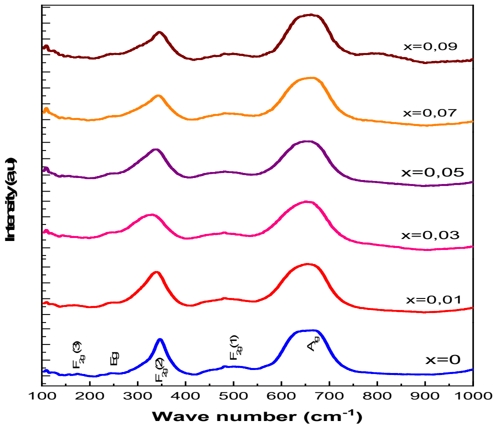

**Figure 5.** Raman measurements of the $ZnFe_{2-x}Yb_xO_4$ (x = 0 0.01 0.03 0.05 0.07 and 0.09) nanoparticles under an excitation $\lambda_{ex}$ = 532nm

All spectra show two noticeable strong bands, common characteristics of spinel structure, where the first around 400-450 cm$^{-1}$ characteristic of octahedral coordinated Fe-O, and the second is more intense in the range 530-600 cm$^{-1}$ associated with the vibrations of the tetrahedral coordinated Zn-O.

The absorption band of octahedral coordination shifts toward higher frequency for the substituted samples, whereas that of tetrahedral varies more less and remains nearly constant (Figure 4). The shifting toward to the higher frequency confirms that Yb$^{3+}$ ions are predominantly replacing Fe$^{3+}$ ions at octahedral sites. This was found with ytterbium doping [42]. Furthermore, an absorption band occurs at 1420 cm$^{-1}$ because of the existence of O–H stretching vibration of free water molecules [43].

The nanopowders ZnFe$_{2-x}$Yb$_x$O$_4$ with (x=0 0.01 0.03 0.05 0.07 and 0.09) have been characterized by Raman scattering in the range of 100 to 1000 cm$^{-1}$ at the wavelength excitation $\lambda_{ex}$ =532nm which crystallize in cubic ferrites. Figure 5 shows Raman spectra which indicate the strongest active mode at 655cm$^{-1}$ corresponding to A$_g$ symmetric stretching mode which it associated to vibration of Zn-O in tetragonal site, in other hand the Fe-O vibrations were attributed at 165-250 and 355 cm$^{-1}$ on octahedral site corresponding to: translational movement of the assembly tetrahedron; F$_{2g}$ (1), symmetric bending; E$_g$ and asymmetric bending; F$_{2g}$ (2) respectively, while the F$_{2g}$ (3) mode at 480 cm$^{-1}$ is the second order active mode Raman. The intensity peaks related to the concentration of Yb$^{3+}$ may be due to the electronegativity values of ytterbium doping as a rare earth and to the length of vibrating bond of ytterbium with environmental atoms in the polyhedron [44-47].

### 3.3. Morphological properties

Scanning electron microscopy (SEM) images of the oxides with compositions x = 0, 0.01, 0.02, 0.03, 0.05, 0.07, and 0.09 are shown in Figure 6. It depicts all powders that consist of micrometric aggregation of smaller particles. The existence of a high-density agglomeration indicates that pore-free crystallites are present on the surface. Nonetheless, for x = 0.02, 0.07, and 0.09, the morphological study reveals the presence of pores and voids due to gases emitted during the synthesis process [48]. Micrographs of ZnFe$_2$O$_4$ samples containing ytterbium are not homogeneous and consist of both monolithic, massive pieces and grains connected by bridges. The samples' irregular shape could result from mechanical grinding [49].

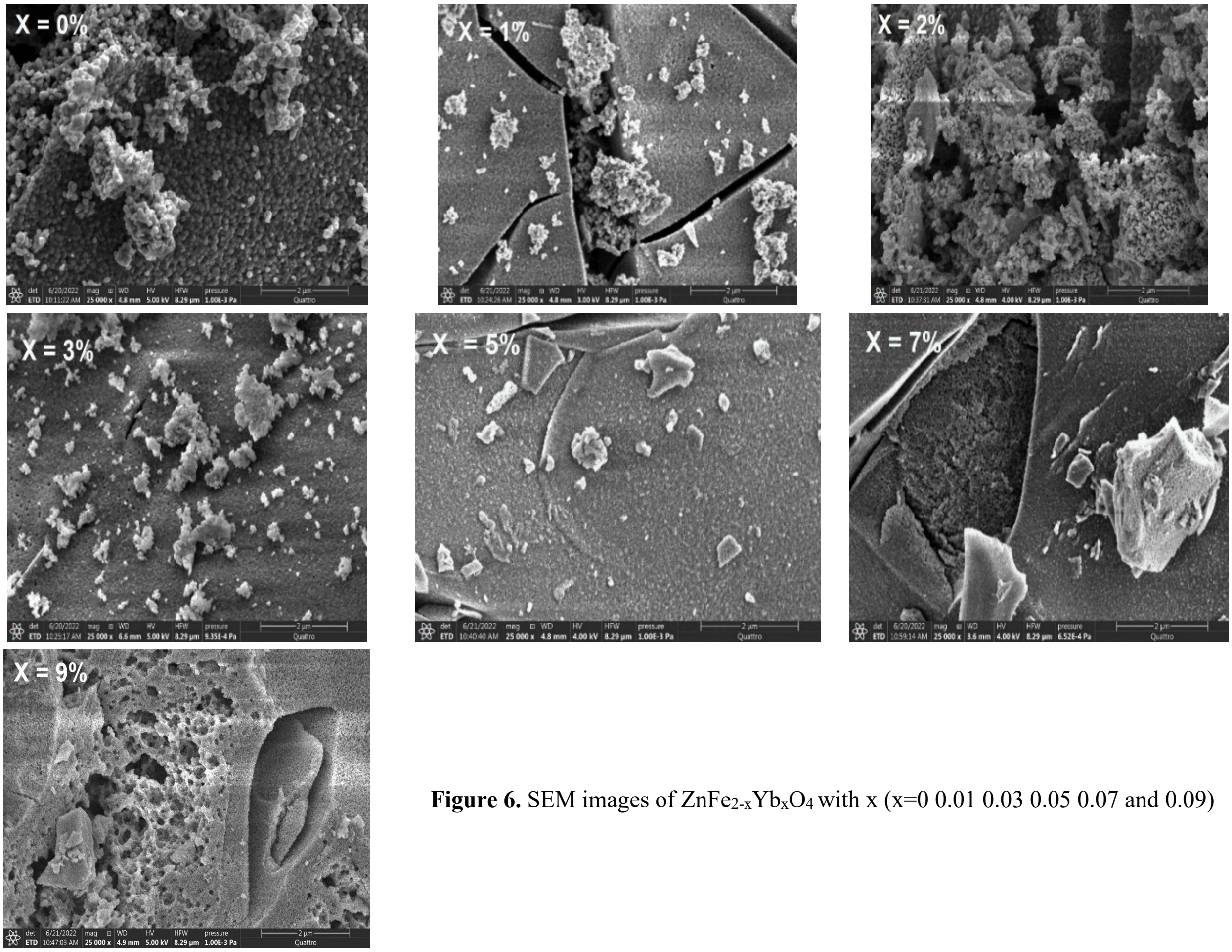

**Figure 6.** SEM images of ZnFe$_{2-x}$Yb$_x$O$_4$ with x (x=0 0.01 0.03 0.05 0.07 and 0.09)

Energy dispersive X-rays analysis was applied to provide the elemental identification and quantitative compositional in formation. Figure 7 shows that all the elements are present, no additional peaks are observed indicating the purity of the nanopowders.

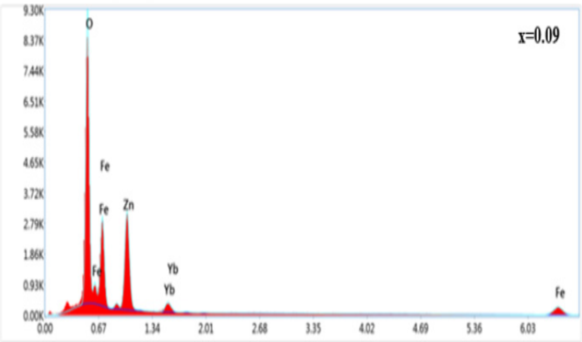

**Figure 7.** EDS analysis for x=0.09

### 3.4. Optical properties

The optical properties of $Yb^{3+}$substituted $ZnFe_2O_4$ spinel nanoparticles were determined using UV–vis analysis.

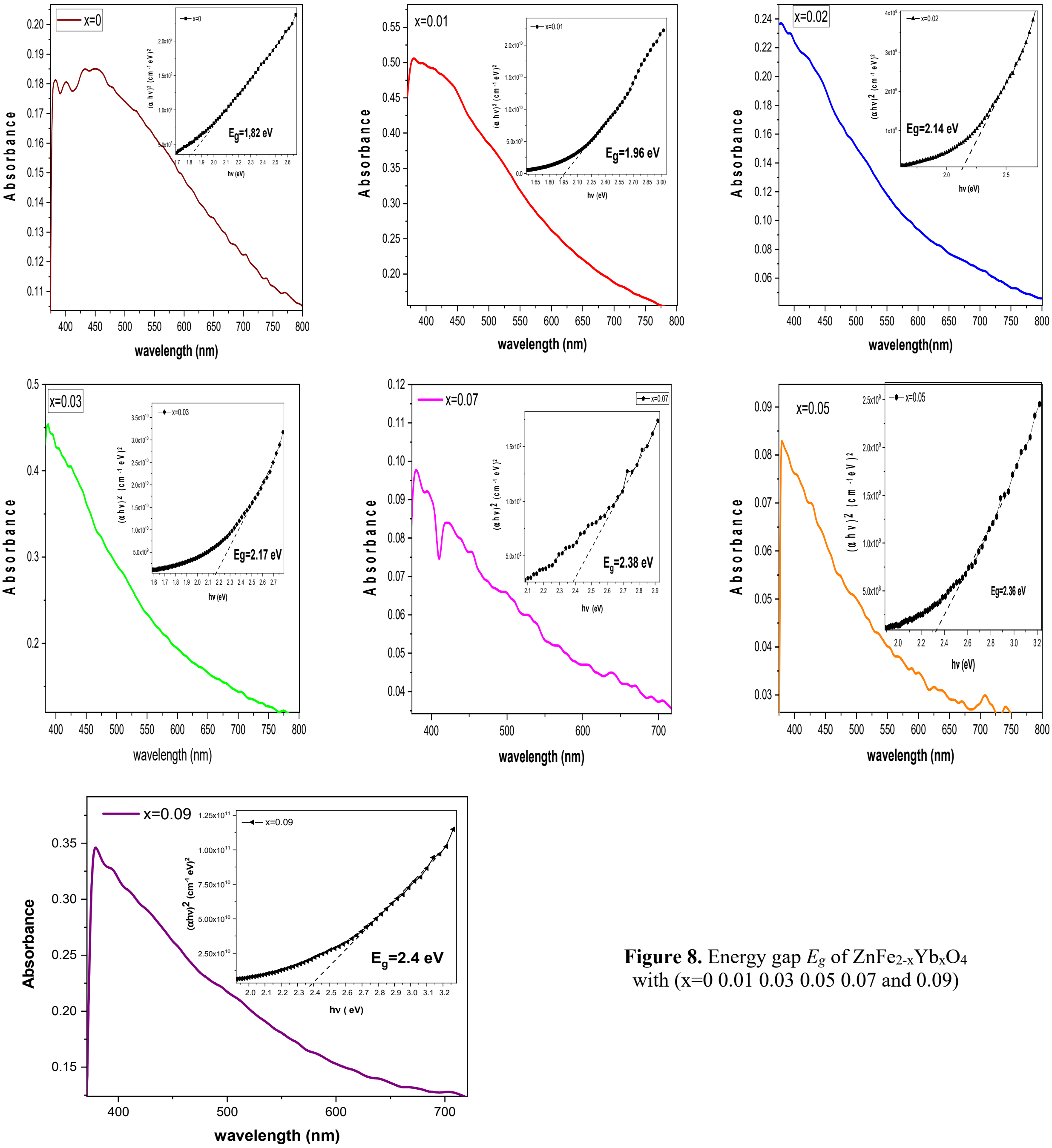

**Figure 8.** Energy gap $E_g$ of $ZnFe_{2-x}Yb_xO_4$ with (x=0 0.01 0.03 0.05 0.07 and 0.09)

Figure 8 shows the energy gap $E_g$ of $ZnFe_{2-x}Yb_xO_4$ at different ratios, which is calculated using the well-known Tauc relation:

$$(\alpha h\nu)^n = A(h\nu - E_g) \tag{4}$$

Where $\alpha$ is the absorption coefficient, $h\nu$ is the photon energy (eV), $A$ is proportionality constant and $n$ are either 2 or 1/2 for direct and indirect transitions, respectively. By extrapolating the linear part of the curve on the energy axis, more reliable values of the gap were determined.

For all samples, the diffuse reflectance spectra exhibit a steep shape of absorption bands characteristic of direct transitions (Figure 8), with an appropriate adjustment for $n = 2$ and is the energy required for electrons to be excited from the top of the valence band (VB) to the bottom of the conduction band (CB) without phonon assistance.

The calculated gaps depend on the $Yb^{3+}$ concentration and increase monotonically with Yb3+ substitution into the crystal lattice, corroborating the existence of a solid solution. This result can be explained by the fact that the $Yb^{3+}$ ions substitution process requires a higher energy level to excite an electron from the valence band to the conduction band, thus increasing the energy band gap of the doped-zinc ferrite. The obtained bandgap energy values for $ZnFe_{2-x}Yb_xO_4$ nanoparticles are comparable to those reported in the literature [35,50-51].

## CONCLUSIONS

In the present work, $Yb^{3+}$ doped $ZnFe_2O_4$ with (x= 0, 0.01, 0.02, 0.03, 0.05, 0.07, and 0.09) have been successfully synthesized by the sol-gel method at 750°C for 8 hours. The obtained powders were then analysed for their structural, morphological, and optical properties. XRD patterns show that $ZnFe_{2-x}Yb_xO_4$ samples are single-phase and crystallize in cubic symmetry with good crystallinity. As the ytterbium ion content increased, the lattice constant increased, whereas the crystallite size decreased from 29 to 104 nm. The specific surface area of the Brunauer–Emmett–Teller (BET) of the $Zn_xFe_{2-x}Yb_xO_4$ (x=0.03) was determined to be the larger 13.59m$^2$/g. FTIR analysis shows that the substitution of ytterbium ions shifts the lower band absorption towards the higher frequency side, indicating the occupancy of $Yb^{3+}$ ions in octahedral sites. The appearance of all active modes in the Raman spectra shows that the structure of spinel ferrite was not changed by the insertion of ytterbium. The SEM images show that the samples are agglomerated and irregular in shape, which could be due to mechanical grinding. The identification and quantitative composition in formation were determined by energy dispersive X-rays (EDS), confirming that all samples contain Zn, Fe, Yb and O without any additional elements. The narrow-bandgap energy is found to be dependent on the ytterbium content and increases monotonically from 1.82 to 2.4 eV with Yb3+ substitution, corroborating the existence of the $ZnFe_{2-x}Yb_xO_4$ samples.

### Acknowledgments

The authors thank the General Directorate of Scientific Research and Technological Development (DGRSDT) for providing the financial support the chemical and physical analysis. Additionally, the authors thank CRAPC LAGHOUAT for physical and chemical examinations. The authors also give acknowledgement to researchers of Laboratory of Physical-Chemical Inorganic Materials and Their Applications (LPCMIA) at Saad Dahleb Blida 1 university, Algeria's.

### ORCID

**Mohammed Guettaf,** https://orcid.org/0009-0005-3875-3782; **Souad Saadi,** https://orcid.org/0009-0002-0633-9294
**Dalila Mouattah,** https://orcid.org/0009-0000-0941-7740; **Amina Kezzim,** https://orcid.org/0000-0001-6638-0809
**Imane Lanez,** https://orcid.org/0000-0001-6758-9583; **Brahim Rekik,** https://orcid.org/0000-0003-4944-3390

## REFERENCES

[1] Gao J, Si F, Wang F, Li Y, Wang G, Zhao J, Ma Y, Yu R, Li Y, Jin C, Li D 2023 *Solid State. Sci.* **135** 107066 https://doi.org/10.1016/j.solidstatesciences.2022.107066
[2] Rahimi S, Nezhad S. M, Zare, E. N, Pourmousavi S. A, Boroujerdian M, Hosseini S 2023 *Inorganic Chemistry Communications* **158** 111556. https://doi.org/10.1016/j.inoche.2023.111556
[3] P. Abishad, M. Jayashankar, A. Hezam, B.S. Srinath, N.V. Kurkure, S.B. Barbuddhe, and R.D.B, Vergis, J. Nano-Structures & Nano-Objects, **37**, 101112 (2024). https://doi.org/10.1016/j.nanoso.2024.101112
[4] R. Jasrotia, Suman, A. Verma, R. Verma, J. Ahmed, S.K. Godara, G. Kumar, *et al.*, J. Water Process Eng. **48**,102865 (2022). https://doi.org/10.1016/j.jwpe.2022.102865
[5] M.A. Gavrilova, D.A. Gavrilova, S.K. Evstrop'ev, and N.V. Nikonorov, Russian Journal of Inorganic Chemistry, 1 (2024). https://doi.org/10.1134/S0036023623602994
[6] R. Jasrotiaa, N. Jaswal, J. Prakasha, C.C. Kit, J. Singhd, and A. Kandwal, Journal of Magnesium and Alloys, **12**, 490 (2024). https://doi.org/10.1016/j.jma.2024.02.006
[7] A. Boujemaa, R. Bouareb, S. Saadi, A. Bouguelia, and M. Trari, Applied Energy, **86**, 1080 (2009). https://doi.org/10.1016/j.apenergy.2008.06.007
[8] S. Attia, N. Helaïli, Y. Bessekhouad, and M. Trari, A: Chemistry, **426**, 113745 (2022). https://doi.org/10.1016/j.jphotochem.2021.113745
[9] Y. Qu, D. Zhang, X. Wang, H. Qiu, T. Zhang, M. Zhang, G. Tian, *et al.*, J. Alloys Compd. **721**, 697 (2017). https://doi.org/10.1016/j.jallcom.2017.06.031
[10] D. Zhang, C. Zhang, H. Xu, Z. Huo, X. Shi, B. Luo, G. Liu, *et al.*, Journal of Alloys and Compounds, **987**, 174212 (2024). https://doi.org/10.1016/j.jallcom.2024.174212

[11] L. Dong, Z. Wang, C. Mi, W. Zhao, C. Qin, C. Luo, and Z. Wang, Materials Today Chemistry, **35**, 101853 (2024). https://doi.org/10.1016/j.mtchem.2023.101853
[12] A.S. Mokrushin, N.P. Simonenko, T.L. Simonenko, E.P. Simonenko, V.G. Sevast'yanov, and N.T. Kuznetsov, Russ. J. Inorg. Chem. **66**, 1425 (2021). https://doi.org/10.1134/S0036023621090060
[13] R. Prakshale, S. Bangale, M. Kamble, and S. Sonawale, Micro and Nanostructures, **189**, 207820 (2024). https://doi.org/10.1016/j.micrna.2024.207820
[14] O.D. Dastjerdi, H. Shokrollahi, and S. Mirshekari, Inorganic Chemistry Communications, **153**, 110797 (2023). https://doi.org/10.1016/j.inoche.2023.110797
[15] J. Wan, X. Jiang, H. Li, and K.J. Mater. Chem. **22**, 13500 (2012). https://doi.org/10.1039/C2JM30684K
[16] B. Hu, Y. Cui, X. Yang, X. Xu, B.J. Janani, and A. Fakhri, Surfaces and Interfaces, **33**, 102226 (2022). https://doi.org/10.1016/j.surfin.2022.102226
[17] M. Srivastava, S.K. Alla, S.S. Meena, N. Gupta, R.K. Mandala, and N.K. Prasad, New J. Chem. **42**(9), 7144 (2018). https://doi.org/10.1039/C8NJ00547H
[18] M. Tahir, M. Fakhar-e-Alam, M. Asif, M.J. Iqbal, A. Abbas, M. Hassan, *et al.*, Heliyon, **10**, (2024) https://doi.org/10.1016/j.heliyon.2024.e24792
[19] E.A. Alghamdi, and R. Sai, Results in Physics, **59**, 107549 (2024). https://doi.org/10.1016/j.rinp.2024.107549
[20] M. Madhu, A.V. Rao, D. Parajuli, S.Y. Mulushoa, and N. Murali, Inorganic Chemistry Communications, **143**, 109818 (2022). https://doi.org/10.1016/j.inoche.2022.109818
[21] H.M.N.H.K. Asghar, M. Khalid, Z.A. Gilani, M. Shifa, A. Parveen, M.S. Ahmed, J.K. Khan, *et al.*, Optical and Quantum Electronics, **53**, 677 (2021). https://doi.org/10.1007/s11082-021-03299-8
[22] G.R. Vasudha, N. Yerol, E. Jomy, and K.V. Anupriya, Materials Today: Proceedings, **2023**, (2023). https://doi.org/10.1016/j.matpr.2023.06.333
[23] R.V. Bharathi, M.K. Raju, P.S.V. Shanmukhi, M.G. Kiran, N. Murali, D. Parajuli, T.W. Mammo, and K. Samatha, Inorganic Chemistry Communications, **158**, 111713 (2023). https://doi.org/10.1016/j.inoche.2023.111713
[24] P. Naik, R.B. Tangsali, S.S. Meena, and S.M. Yusuf, Materials Chemistry and Physics, **191**, 215 (2017). https://doi.org/10.1016/j.matchemphys.2017.01.032
[25] H. Javeda, F. Iqbalb, P.O. Agboolac, M.A. Khanb, M.F. Warsia, and I. Shakird, Ceramics International, **45**, 11125 (2019). https://doi.org/10.1016/j.ceramint.2019.02.176
[26] S. Nadaf, B. Chethan, K.M. Swathi, S.S. Laxmeshwar, J. Angadi, K. Manjunatha, V. Molahalli, *et al.*, Ceramics International, (2024). https://doi.org/10.1016/j.ceramint.2024.04.045
[27] S.E. Jacobo, S. Duhalde, and H.R. Bertorello, Journal of Magnetism and Magnetic Materials, **276**, 2253 (2004). https://doi.org/10.1016/j.jmmm.2003.12.564
[28] M.M. Baig, S. Zulfiqar, M.A. Yousuf, M. Touqeer, S. Ullah, P.O. Agboola, M.F. Warsi, and I. Shakir, Ceram. Int. **46**, 23208 (2020). https://doi.org/10.1016/j.ceramint.2020.06.103
[29] P. Priyadharshini, and K. Pushpanathan, Chemical Physics Impact, **6**, 100201 (2023). https://doi.org/10.1016/j.chphi.2023
[30] M. Choupani, and A, Gholizadeh, Journal of rare earth, (2023). https://doi.org/10.1016/j.jre.2023.06.011
[31] M. Vucinic-Vasic, E.S. Bozin, L. Bessais, G. Stojanovic, U. Kozmidis-Luburic, M. Abeykoon, B. Jancar, *et al.*, J. Phys. Chem. C, **117**, 12358 (2013). https://doi.org/10.1021/jp403459t
[32] G. Wang, Y. Ma, Y. Tong, X. Dong, and M. Li, J. Intell. Mater. Syst. Struct. **28**(17), 2331 (2017). https://doi.org/10.1177/1045389X16685449
[33] J.N. Baby, C. Lavanya, S. Wang, B. Sriram, A. Anantharaman and M. George, New J. Chem. 45 (2021) 10049–10056. https://doi.org/10.1039/D1NJ01367J
[34] H. Ghorbani, M. Eshraghi, A.S. Dodaran, P. Kameli, S. Protasowicki, and D. Vashaee, Materials Research Bulletin, **147**, 111642 (2022). https://doi.org/10.1016/j.materresbull.2021.111642
[35] M.R. Rather, A.M, Sultan, S. Khalid, S. Abass, and R. Samad, Journal of Sol-Gel Science and Technology, **1,** (2024). https://doi.org/10.1007/s10971-024-06362-4
[36] S.R. Naik, and A.V. Salker, Journal of Alloys and Compounds, **600**, 137 (2014). http://dx.doi.org/10.1016/j.jallcom.2014.02.101
[37] A. Hakimyfard, and S. Mohammadi, Adv. Powder Technol. **30**, 1257 (2019). https://doi.org/10.1016/j.apt.2019.04.005
[38] D.D. Andhare, S.A. Jadhav, M.V. Khedkar, S.B. Somvanshi, S.D. More, and K.M. Jadhav, Journal of Physics: Conference Series, **1644**, 012014 (2020). https://doi.org/10.1088/1742-6596/1644/1/012014
[39] N Koriche, A. Bouguelia, and M. Trari, International Journal of Hydrogen Energy, **80**, 272 (2006). https://doi.org/10.1016/j.ijhydene.2004.06.011
[40] Z. Li, G. Chen, X. Tian, and Y. Li, Res. Bull. **43**, 1781 (2008). https://doi.org/10.1016/j.materresbull.2007.07.010
[41] S. Saadi, A. Kezzim, A. Irekti, M.S. Nas, and M. Guettaf, Russ. J. Gen. Chem. **94**, 1207 (2024). http://dx.doi.org/10.1134/S1070363224050189
[42] A.B. Gadkari, T.J. Shinde, and P.N. Vasambekar, Materials Chemistry and Physics, **114**, 505 (2009). https://doi.org/10.1016/j.matchemphys.2008.11.011
[43] S. Yuvaraj, S. Revathi, A. Kumar, G. Anitha, A.M. Al-Enizi, B. Pandit, R. Revathi, *et al.*, Optical Materials, **145**, 114423 (2023). https://doi.org/10.1016/j.optmat.2023.114423
[44] A. Aslam, N.A. Morley, N. Amin, M.I. Arshad, M.A. Nabi, A. Ali, K. Mahmood, *et al.*, Physica B: Physics of Condensed Matter, **601**, 412565 (2021). https://doi.org/10.1016/j.physb.2020.412565
[45] N.B. Singh, and A. Agarwal, Materials Today: Proceedings, **5**, 9148 (2018). https://doi.org/10.1016/j.matpr.2017.10.035
[46] A. Manohar, C. Krishnamoorthi, K.C.B. Naidu, and C. Pavithra, Applied Physics A, **125**, (2019). https://doi.org/10.1007/s00339-019-2760-0
[47] Z.Ž. Lazarević, Č. Jovalekić, A. Milutinović, D. Sekulić, V.N. Ivanovski, A. Rečnik, B. Cekić, and N.Ž. Romčević, Journal of Applied Physics **113**, 187221 (2013). http://dx.doi.org/10.1063/1.4801962
[48] N.M. Deraz, Journal of Alloys and Compounds, **501**(2), 317 (2010). https://doi.org/10.1016/j.jallcom.2010.04.096

[49] C. Aziz, and B. Azhdar, Journal of Magnetism and Magnetic Materials, **542**, 168577 (2022). https://doi.org/10.1016/j.jmmm.2021.168577

[50] R.S. Yadav, I. Kuřitka, J. Vilcakova, P. Urbánek, M. Machovsky, M. Masař, and M. Holek, Journal of Physics and Chemistry of Solids, **110**, 87 (2017). https://doi.org/10.1016/j.jpcs.2017.05.029

[51] M. Shobana, T. Raguram, N. Eswaramoorthy, G. Cárdenas-Jirón, K. Granados-Tavera, and A.N. Alodhayb, *et al*., Ceramics International, **51**(5), (2025). https://doi.org/10.1016/j.ceramint.2024.12.119

## ДОСЛІДЖЕННЯ ФІЗИЧНИХ ВЛАСТИВОСТЕЙ НАНОПОРОШКІВ $ZnFe_2O_4$, ЛЕГОВАНИХ $Yb^{3+}$, СИНТЕЗОВАНИХ ЗОЛЬ-ГЕЛЬ МЕТОДОМ

**М. Геттаф[1], С. Сааді[2], Д. Муаттах[3], А. Кеззім[1], І. Ланез[1], Б. Рекік[1]**
*[1]Лабораторія фізико-хімічних неорганічних матеріалів та їх застосування (LPCMIA), Університет Саада Далеба,*
*Бліда 1, BP270 09000, Бліда, Алжир*
*[2]Лабораторія прикладної хімії та матеріалів (LabCAM), Університет Мхамеда Бугари в Бумердесі,*
*Авеню де л'Індепенданс, Бумердес, 35000. Алжир*
*[3]Лабораторія фізико-хімії матеріалів (LPCM), Університет Амар Теліджі, BP37G 03000, Лагуат, Алжир*

$ZnFe_{2-x}Yb_xO_4$ з (x = 0, 0,01, 0,02, 0,03, 0,05, 0,07 та 0,09) були успішно синтезовані золь-гель методом при 750°C. Результати рентгенівської дифракції показали однофазні та кристалічні нанопорошки зі структурою шпінелі з кубічною симетрією та просторовою групою . Параметри решітки збільшуються зі збільшенням концентрації $Yb^{3+}$. Питома площа $Zn_xFe_{2-x}Yb_xO_4$ за методом BET (x = 0,03) була визначена як більша з них і становить 13,59 м²/г. Розмір кристалітів, визначений Рітвельдом, знаходиться в діапазоні 29-104 нм. ІЧ-спектри з Фур'є показали дві сильні смуги поглинання, що є загальною характеристикою структури шпінелі. Крім того, зміщення нижньої смуги поглинання в бік вищої частоти підтверджує, що іони Yb3+ переважно заміщують іони $Fe^{3+}$ в октаедричних позиціях. Формування шпинельної фази у зразках також було підтверджено за допомогою комбінаційного розсіювання з асиметричним розширенням, і спостерігався систематичний зсув у спектрах комбінаційного розсіювання як функція концентрації $Yb^{3+}$. Скануюча електронна мікроскопія SEM показала, що порошки складаються з мікрометричної агрегації дрібніших частинок. EDS-дослідження підтвердили, що хімічні елементи Zn, Fe, Yb та O присутні у всіх зразках. Значення прямої енергії забороненої зони розраховані за графіком Таука, і це вказує на напівпровідниковий характер нашої сполуки, демонструючи збільшення та посилення значень енергії забороненої зони від 1,82 до 2,4 еВ із заміщенням $Yb^{3+}$.

**Ключові слова:** *ітербій; нанопорошки фериту цинку; рентгенівська дифракція; Раман; енергія забороненої зони*